

Exploring dopant effects in stannic oxide nanoparticles for CO₂ electro-reduction to formate

Young-Jin Ko ^{1,9}✉, Jun-Yong Kim^{2,3,9}, Woong Hee Lee ^{1,9}, Min Gyu Kim ⁴, Tae-Yeon Seong³, Jongkil Park⁵, YeonJoo Jeong ⁵, Byoung Koun Min ^{1,6}, Wook-Seong Lee², Dong Ki Lee ^{1,6,7}✉ & Hyung-Suk Oh ^{1,7,8}✉

The electrosynthesis of formate from CO₂ can mitigate environmental issues while providing an economically valuable product. Although stannic oxide is a good catalytic material for formate production, a metallic phase is formed under high reduction overpotentials, reducing its activity. Here, using a fluorine-doped tin oxide catalyst, a high Faradaic efficiency for formate (95% at 100 mA cm⁻²) and a maximum partial current density of 330 mA cm⁻² (at 400 mA cm⁻²) is achieved for the electroreduction of CO₂. Furthermore, the formate selectivity (≈90%) is nearly constant over 7 days of operation at a current density of 100 mA cm⁻². *In-situ/operando* spectroscopies reveal that the fluorine dopant plays a critical role in maintaining the high oxidation state of Sn, leading to enhanced durability at high current densities. First-principle calculation also suggests that the fluorine-doped tin oxide surface could provide a thermodynamically stable environment to form HCOO* intermediate than tin oxide surface. These findings suggest a simple and efficient approach for designing active and durable electrocatalysts for the electrosynthesis of formate from CO₂.

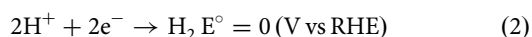
¹Clean Energy Research Center, Korea Institute of Science and Technology (KIST), Hwarang-ro 14-gil 5, Seongbuk-gu, Seoul 02792, Republic of Korea.

²Electronic Materials Research Center, Korea Institute of Science and Technology (KIST), Hwarang-ro 14-gil 5, Seongbuk-gu, Seoul 02792, Republic of Korea.

³Department of Materials Science and Engineering, Korea University, Seoul 02841, Republic of Korea. ⁴Beamline Research Division, Pohang Accelerator Laboratory (PAL), Pohang 37673, Republic of Korea. ⁵Center for Neuromorphic Engineering, Korea Institute of Science and Technology (KIST), Hwarang-ro 14-gil 5, Seongbuk-gu, Seoul 02792, Republic of Korea. ⁶Graduate School of Energy and Environment (Green School), Korea University, 145 Anam-ro, Seongbuk-gu, Seoul 02841, Republic of Korea. ⁷Division of Energy and Environmental Technology, KIST school, Korea University of Science and Technology, Seoul 02792, Republic of Korea. ⁸KIST-SKKU Carbon-Neutral Research Center, Sungkyunkwan University, 2066 Seobu-ro, Jangan-gu, Suwon 16419, Republic of Korea. ⁹These authors contributed equally: Young-Jin Ko, Jun-Yong Kim, Woong Hee Lee. ✉email: 091183@kist.re.kr; dnklee@kist.re.kr; hyung-suk.oh@kist.re.kr

⁹These authors contributed equally: Young-Jin Ko, Jun-Yong Kim, Woong Hee Lee. ✉email: 091183@kist.re.kr; dnklee@kist.re.kr; hyung-suk.oh@kist.re.kr

The catalytic conversion of CO₂ to fuels or valuable chemical products provides a carbon-neutral cycle that can mitigate the rapid consumption of fossil resources and increasing CO₂ emissions^{1,2}. Recently, in accordance with global CO₂ reduction regulations, carbon capture utilization and storage (CCUS) technology for large-scale greenhouse gas reduction and conversion to high-value-added products has been intensively researched. In particular, the electrocatalytic reduction of CO₂ has attracted interest owing to recent developments in electricity production from renewable energy sources such as solar and wind^{3,4}. As a widely used raw material in the pharmaceutical, tanning, and textile industries that can also act as a hydrogen carrier for fuel cells⁵, formate is a very attractive product of the CO₂ reduction reaction (CO₂RR). Furthermore, given the required energy input and the market price of formate, the electrochemical reduction of CO₂ to formate is an economically valuable process⁶. Various studies on the use of heteroatom-doped/alloy catalysts or catalyst structures with large active areas for the electrocatalytic reduction of CO₂ to formate have been reported^{7–11}. However, a highly efficient catalyst that can meet commercial requirements for activity, selectivity, and stability has not yet been achieved.



Until now, metal-based catalysts have generally been used for CO₂ electroreduction because of their high activity and stability^{12–21}. As the CO₂RR to formate (Eq. 1) competes with the hydrogen evolution reaction (HER; Eq. 2), inhibiting the HER is essential for obtaining a high selectivity for formate. According to Trassati's volcano plot²², metals such as Pb²³, Bi²⁴, In²⁵, Hg²⁴, and Sn²³, which are generally located on the left branch of the volcano plot, exhibit high CO₂RR selectivity for formate. The weak metal–hydrogen bonds of these metals result in good CO₂RR activity for formate production.

Among these materials, Sn is the most reasonable material because the toxicity (Pb, Hg) or relatively scarcity in the earth's crust (Bi) of other typical catalyst materials limit their commercialization²⁶. Considerable efforts have been focused on developing Sn-based catalysts for formate production, with recent advances including the use of gaseous CO₂ flow cells^{27–40}. Although improvements in the catalytic activity for formate production have been achieved, the long-term durability of Sn-based catalysts under reduction conditions remains a critical issue (Supplementary Table 1). Previous research has indicated that a Sn species with a high oxidation state is key for achieving high catalytic activity for the CO₂RR to formate^{41,42}. Bocarsly et al. observed intermediates on the Sn electrode by *in situ* infrared spectroscopy and suggested that the oxidized Sn surface is a catalytically active species for the CO₂RR⁴³. However, Sn electrocatalysts with high oxidation states are reduced at high reduction overpotentials during the CO₂RR, resulting in the formation of a metallic phase and the loss of catalytic activity⁴¹. This phenomenon can be suppressed under strongly alkaline conditions, but alkaline electrolytes, such as potassium hydroxide (KOH), can be neutralized during CO₂RR due to the purging of CO₂. Therefore, it is necessary to develop alternative Sn-based electrocatalysts to ensure stability at high current densities.

Here, we studied a fluorine-doped tin oxide (FTO) nanocatalyst that not only showed high CO₂RR activity over a wide range of current densities but also maintained its performance for more than a week. The electrochemical CO₂RR performance is significantly affected by the device design and the type of purged CO₂^{44,45}. Therefore, a homemade gaseous CO₂ fed flow cell was used to achieve a high current density. *In-situ/operando* analysis

was conducted under similar conditions. We found that replacing Sn–O bonds with Sn–F bonds promotes the interactions of catalyst surface and HCOO[−], and modified electronic structure of CO₂ to facilitate electron transfer. The F dopant was also revealed to play a significant role in maintaining the oxidation state of Sn at high reduction overpotentials. This work provides an advanced strategy for synthesizing cost-effective CO₂RR electrocatalysts with high activity and selectivity.

Results

Structure and physical properties of stannic oxide electrocatalysts. SnO₂, fluorine-doped-SnO₂ (FTO), antimony-doped tin oxide (ATO), and indium-doped tin oxide (ITO) nanoparticles supported on carbon black were synthesized using a sol-gel method with hydrothermal treatment. The overall synthesis scheme is illustrated in Fig. 1a and includes the following steps:⁴⁶ (1) formation of a metal-surfactant complex, (2) hydrolysis and condensation, (3) formation of a micelle-like surfactant template with a SnO₂ phase, and (4) hydrothermal treatment for crystallization. The mechanism is described in more detail in Supplementary Note 1. Figure 1b, c and Supplementary Fig. 1 shows high-resolution transmission electron microscopy (HR-TEM) images of the synthesized SnO₂ and doped-SnO₂ catalysts with corresponding particle size distributions (insets, Fig. 1b, c). The SnO₂ and doped-SnO₂ samples consist of very small oxide clusters (<5 nm) with uniform distributions. All the catalysts had similar average particle sizes [2.567 nm (SnO₂), 2.121 nm (FTO), 2.391 nm (ITO), and 2.154 nm (ATO)], and the dopants were uniformly distributed in the doped-SnO₂ particles (Supplementary Figs. 2–4). On the contrary, while the SnO₂ catalyst without tetradecylamine (TDA) surfactant has a similar particle size compared to SnO₂ with TDA surfactant (2.603 nm, Supplementary Fig. 5), it aggregated to show a disordered mesoporous structure.

The SnO₂ and doped-SnO₂ nanoparticles all exhibited rutile tetragonal crystal structures, as identified by analyzing the zone axis of the images^{47,48}. Furthermore, the crystal structures and average particle sizes of the synthesized nanoparticles were analyzed using X-ray diffraction (XRD) (Fig. 1d). In the XRD patterns, the (110), (101), and (211) reflections of tetragonal SnO₂ were observed at 2θ values of 26.3°, 33.6°, and 51.9°, respectively^{46,49}. The quality of the synthesized SnO₂ and doped-SnO₂ catalysts was analyzed by thermogravimetric analysis (TGA) (Supplementary Fig. 6). All the catalysts showed a weight loss of ~20% from 30 to 500 °C owing to the removal of adsorbed water molecules and stable oxygen functional groups in the carbon support^{50,51}. Under flowing O₂, the catalyst weight slightly increased and then decreased rapidly, which was attributed to complete oxidation of the carbon support to CO₂ gas after the formation of oxygen functional groups. The SnO₂ and doped-SnO₂ catalysts were both found to have oxide contents of approximately 40 wt%. The similarities in the morphologies, crystal structures, and oxide contents of the SnO₂ and doped-SnO₂ nanoparticles allowed comparisons of their catalytic activities and efficiencies for CO₂ reduction to formate under the same conditions.

CO₂-to-formate conversion performance. The electrochemical CO₂RR activities of the SnO₂-based catalysts were evaluated in a homemade flow cell using gaseous CO₂ to accelerate the CO₂RR while minimizing the mass transfer resistance. A detailed schematic of the flow cell is shown in Fig. 2a and Supplementary Fig. 7. The SnO₂-based catalysts were loaded onto a gas diffusion layer (GDL) and gaseous CO₂ was supplied to the cathode. An electrolyte of 1 M KOH or 1 M KHCO₃ was used in both the

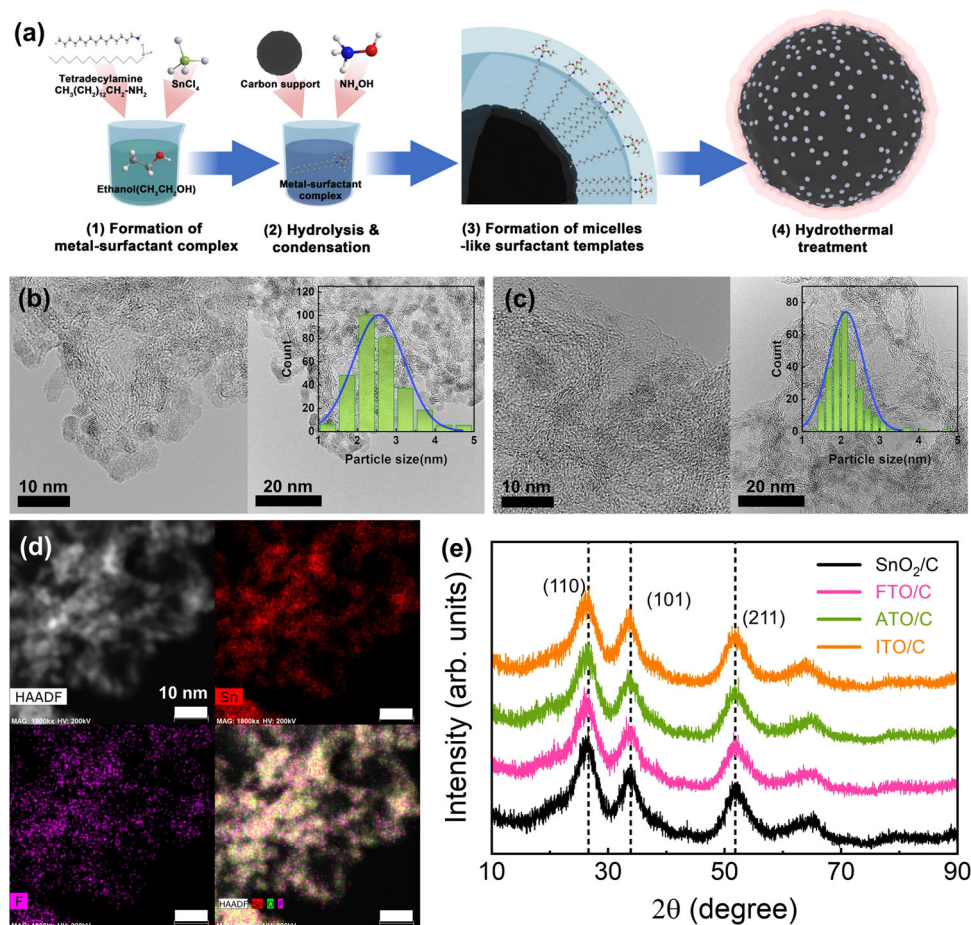


Fig. 1 Physical properties and synthetic scheme of Sn-based catalysts. **a** Synthetic pathway of well-dispersed Sn-based catalysts supported on carbon: (1) formation of metal-surfactant complex, (2) hydrolysis and condensation, (3) formation of micelle-like surfactant templates, and (4) hydrothermal treatment for recrystallization. HR-TEM images of **b** SnO₂/C and **c** FTO/C catalysts (Inset: particle size distributions; average particle sizes and standard deviations fitted with a Gaussian function). **d** HAADF-STEM image and its energy-dispersive X-ray spectroscopy (EDS) mapping images of Sn (red), F (magenta), and layered image combining all maps for FTO/C. The signal collecting time was 5 min. **e** Powder XRD spectra of Sn-based catalysts with various dopants. It indicated that the no phase change occurred by dopants.

cathode and anode flow channels, which were physically separated using an anion exchange membrane (AEM). Supplementary Figure 8a shows the linear sweep voltammetry (LSV) curves for SnO₂/C and SnO₂/C without tetradecylamine (TDA) using 1 M KOH as the electrolyte. SnO₂/C exhibited significantly lower overpotentials than SnO₂/C without TDA. At current densities below 300 mA cm⁻², SnO₂ showed a faradaic efficiency for formate (FE_{formate}) of more than 70% (Supplementary Fig. 8b). In contrast, for SnO₂/C without TDA, FE_{formate} was reduced to 28.6% at 200 mA cm⁻². The maximum formate production rate of SnO₂/C (4.11 mmol h⁻¹ cm⁻²) was almost three times higher than that of SnO₂/C without TDA (1.44 mmol h⁻¹ cm⁻²). The effect of TDA on the SnO₂ particle size before and after CO₂RR is not substantial. However, without TDA, the SnO₂ particles are agglomerated (Supplementary Fig. 9: HR-TEM images of the SnO₂ catalyst with and without TDA). These results show that the uniformity of the SnO₂ particles significantly affects their CO₂RR activity.

To observe the effects of doping on the CO₂RR activity, the electrochemical CO₂RR activities of FTO/C, ATO/C, and ITO/C were compared with that of SnO₂/C (Fig. 2b, c and Supplementary Figs. 8 and 9). All the SnO₂-based electrodes exhibited similar LSV curves, but the electrochemical reaction products differed (Supplementary Fig. 10a). In 1 M KOH solution, FTO/C exhibited an excellent FE_{formate} value of 95% at 100 mA cm⁻²,

which is higher than that of ITO/C (85%), ATO/C (80%), and SnO₂/C (80%). Moreover, FTO/C maintained a FE_{formate} value of more than 90% up to a current density of 300 mA cm⁻². The maximum partial current density and formate production rate of FTO/C were 330 mA cm⁻² and 6.31 mmol h⁻¹ cm⁻², respectively, which are superior to those of ITO/C (272 mA cm⁻², 5.20 mmol h⁻¹ cm⁻²), ATO/C (242 mA cm⁻², 4.62 mmol h⁻¹ cm⁻²), and SnO₂/C (215 mA cm⁻², 4.11 mmol h⁻¹ cm⁻²). These results indicate that F doping of SnO₂ promotes the catalytic activity for the CO₂RR to formate.

To test the stabilities of FTO/C and SnO₂/C, 1 M KHCO₃ was used as the electrolyte. In 1 M KOH, the anolyte is neutralized during the electrochemical CO₂RR, leading to a high overpotential for OER (Supplementary Fig. 11). Considering the stability of the whole system, the CO₂ electrolyzer was optimized for neutral media. At 100 mA cm⁻², the FE_{formate} value of FTO/C was ~90%, whereas that of SnO₂ was 75% (Supplementary Fig. 12). During the stability tests at a current density of 100 mA cm⁻², the FE_{formate} value of SnO₂/C decreased significantly after several hours and the cell potential decreased slightly, showing the low stability of SnO₂/C. In contrast, the cell potential of FTO/C remained stable for 7 days and a FE_{formate} value of ~90% was maintained (Fig. 2e, f). X-ray photoelectron spectroscopy (XPS), HAADF-STEM, and EDS after the stability tests demonstrated that the structure and chemical state of FTO/C

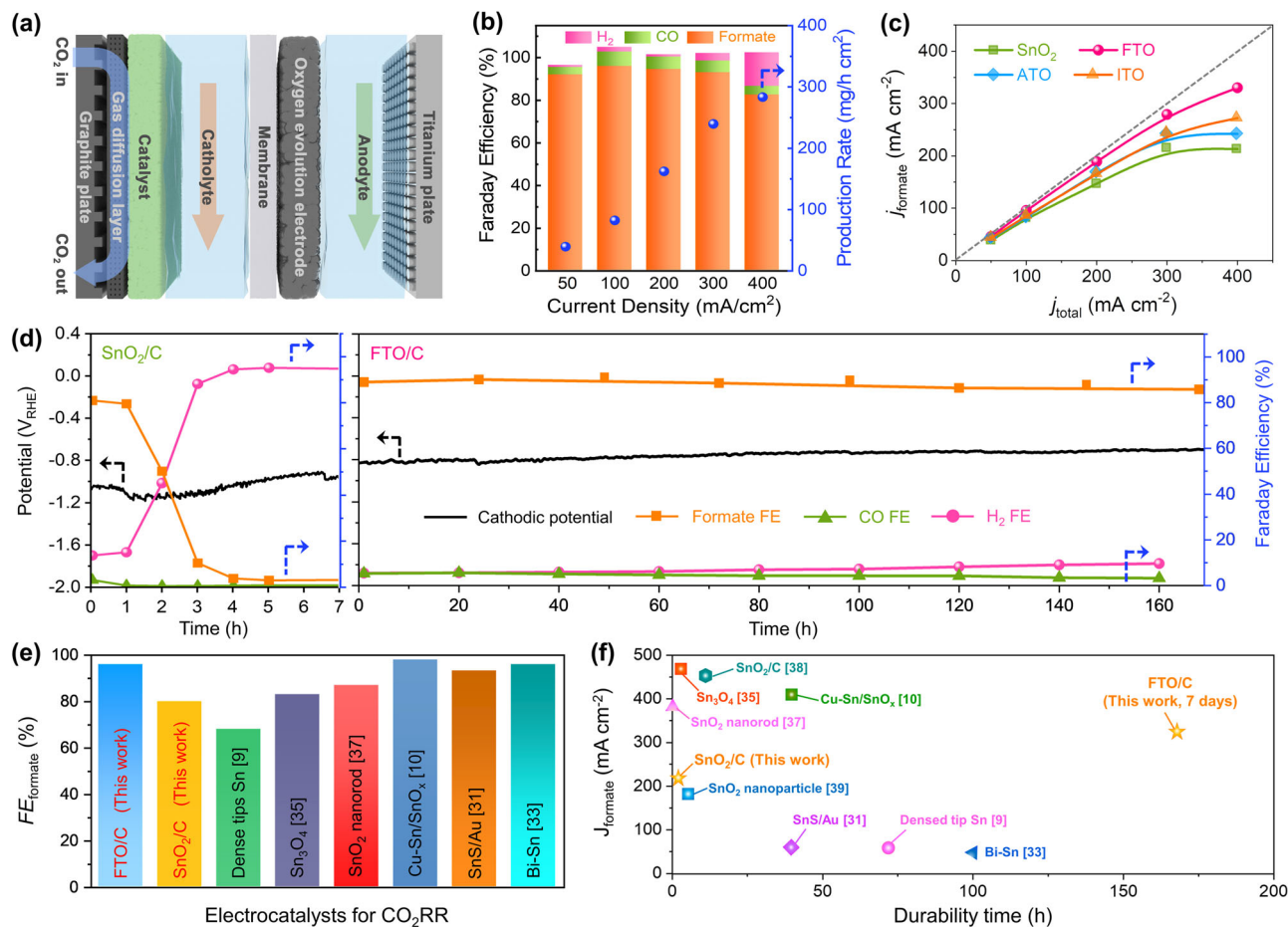


Fig. 2 Single-cell performances of Sn-based catalysts. **a** Schematic of the flow-type CO₂ electrolyzer using a gas-diffusion layer. **b** Faradaic efficiencies of the products and production rates of formate for FTO/C catalyst at each given current density in 1 M KOH solution. **c** Partial current densities of formate for CO₂RR in the current density range of 50–400 mA cm⁻² over those of the synthesized catalysts. The error bar was calculated from three independent tests. **d** Durability test of SnO₂/C (left) and FTO/C (right) catalysts in the flow-type CO₂ electrolyzer in 1 M KHCO₃ solution. The faradaic efficiencies of CO, H₂ and formate reported were observed during the durability test. **e** FE_{formate} of advanced Sn-based CO₂RR catalysts. **f** Plot of the partial current density of formate (mA cm⁻²) versus the durability for various Sn-based CO₂RR electrocatalysts.

remained the same even after the exposure to long-term cathodic conditions (Supplementary Figs. 13 and 14). These results indicate that F doping of SnO₂ provides excellent long-term stability for formate production in a gaseous CO₂-fed flow cell. To evaluate the level of developed catalysts, the activity and stability of the FTO/C catalysts were compared with that of other Sn-based literature catalysts (Fig. 2e, f and Supplementary Table 1). The FTO/C catalysts exhibits comparable FE_{formate} and current density to other best-reported catalysts, indicating enhanced intrinsic catalytic properties for CO₂ electro-reduction to formate. Remarkable durability of FTO/C compared to other literatures suggests that F doping improves stability of Sn catalysts required for real electrochemical formate production.

Theoretical investigation of CO₂-formate conversion on the SnO₂ and FTO surface. The enhanced FE_{formate} of FTO was investigated through density functional theory (DFT) calculations. As the XRD patterns of the as-prepared SnO₂ and FTO nanoparticles did not reveal any preferred orientations, the SnO₂ and FTO surfaces were modeled using a four-layer slab composed of the tetragonal (110) plane. To build the FTO (110) supercell, 15% of the oxygen atoms in the SnO₂ (110) supercell were randomly replaced with fluorine atoms. The elementary steps of the electrochemical conversion reaction of CO₂ to HCOOH involving two electron pathways were described in three steps (Method).

CO₂ adsorption on the catalyst surface was performed to consider the onset potential difference between water and CO₂ reduction. The adsorbed CO₂ (CO₂^{*}) is then converted to the HCOO^{*} intermediate and HCOOH_(g) in sequence with two proton-coupled electron transfers. A recent study demonstrated that, in CO₂ reduction current densities higher than 35 mA cm⁻², the proton can be supplied to CO₂^{*} on the electrode surface by the dissociation of water molecules. At these current density regions, a huge amount of unused hydroxide ions is rapidly generated as a by-product, which results to the increase of the local interfacial pH to values above 12. This is regardless of the type of the buffering agent used⁵². In this regard, the proton for the CO₂ reduction reaction is assumed to be predominantly supplied by the local electrolyte.

For both the SnO₂ and FTO (110) surfaces, the CO₂ molecule was gently adsorbed on the Sn atoms. Then, the HCOO^{*} intermediate was formed as the oxygen atoms of CO₂ were tightly bound to the Sn atoms. The difference between the CO₂ adsorption energies on the SnO₂ and FTO (110) surfaces was not substantial. However, approximately, a 1-eV difference was observed on the free energies for the HCOO^{*} intermediate and HCOOH_(g) formation steps. The FTO surface could provide thermodynamically favorable conditions for HCOO^{*} formation compared to the SnO₂ surface, whereas the conditions on the SnO₂ surface favors the HCOOH_(g) formation (Fig. 3 and

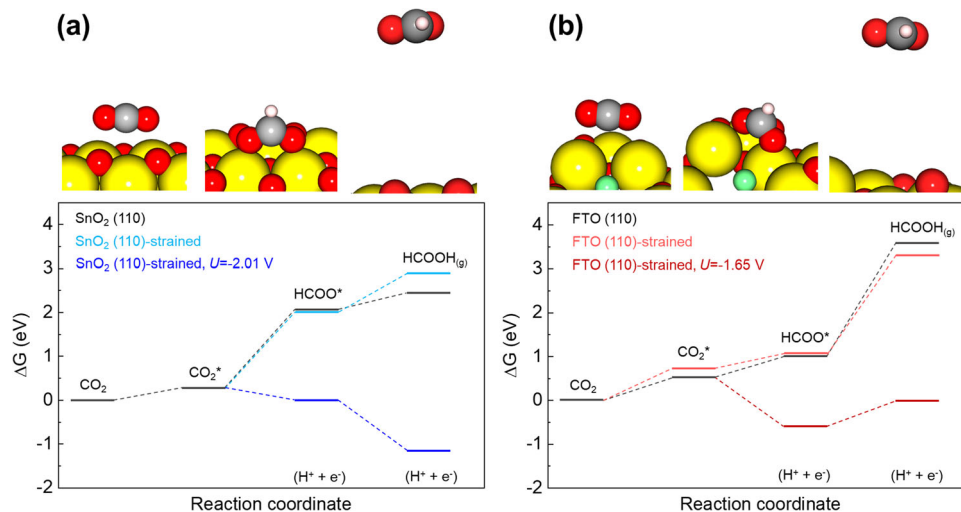


Fig. 3 DFT calculation results of Sn-based catalysts for electrochemical CO₂ conversion to formate. Free energy diagram of CO₂ to HCOOH conversion reaction on the **a** SnO₂ (110) and **b** FTO (110) surface (yellow: Sn, red: O, white: H, green: F). The strained supercells were used to simulate the structural change on SnO₂ and FTO nanoparticles at an applied potential of 1.0 V under CO₂ reduction reaction.

Supplementary Table 2). From the computational hydrogen electrode model, a minimum potential of -2.05 V was required for SnO₂ to overcome the activation barrier of HCOO* formation, whereas -1.79 V was needed for FTO to complete HCOOH_(g) formation. Identical free energy calculations using strained SnO₂ and FTO supercells were performed to simulate the structural changes on the SnO₂ and FTO electrodes during CO₂ reduction. The in-situ EXAFS data demonstrated that the bonding distance between Sn and Sn (or O) was slightly decreased by applying a potential of -1.0 V. Consequently, the lattice constants of the SnO₂ and FTO supercells decreased uniformly by 1.37% and 0.33%, respectively. The observed changes in the lattice constants correspond to the average change of each bonding distance at -1.0 V (Supplementary Fig. 15 and Supplementary Table 3). Although the strained SnO₂ (110) surface registered a lower energy for the formation of HCOOH_(g) by 0.42 eV, the energies for CO₂ adsorption and HCOO* formation were almost identical to those recorded for the SnO₂ surface. As such, the free energy for the HCOO* formation, which is the potential-limiting step, was not affected by the compression of the SnO₂ (110) crystal. In consequence, a potential of more than 2 V was still required for the strained SnO₂. In contrast, the strained FTO (110) surface showed a 0.27-eV lower free energy for the HCOOH_(g) formation, while the energies for CO₂ adsorption and HCOO* formation slightly increased compared to that on the FTO surface. Since the HCOOH_(g) formation is the potential-limiting step for the FTO electrode, the minimum potential to complete the CO₂-to-HCOOH conversion reaction decreased from -1.79 V to -1.65 V as the FTO crystal was compressed. The DFT studies suggest that doping fluorine to SnO₂ could alter the chemical environment of the oxide surface, making it thermodynamically stable for HCOO* intermediate formation, which is an important step in the CO₂-to-HCOOH conversion reaction. In addition, the compression of the crystal through the application of an external bias rendered an effective contribution only for FTO. Therefore, these factors are assumed to facilitate formate production in the FTO electrode.

Origin of excellent durability with high current density under highly reduction potential. In addition to the high FE_{formate} of FTO/C, the high partial current density for formate at high cathodic overpotentials with excellent stability is another major

advantage of this catalyst. To reveal the origin of this behavior, *in-situ/operando* X-ray absorption near-edge structure (XANES) spectroscopy at the Sn k-edge and Raman spectroscopy were performed for SnO₂-based electrodes under gaseous CO₂RR conditions in a customized electrochemical cell with a GDL (Supplementary Figs. 16 and 17). XANES is a bulk-sensitive technique that can reveal the oxidation state of materials, whereas Raman spectroscopy is a surface-sensitive technique that can identify the chemical structure of materials. Therefore, the combination of these *in-situ/operando* spectroscopies can be used to reveal the state of materials during the CO₂RR. The ex-situ Sn k-edge XANES spectrum showed that both catalysts were predominantly in the quadrivalent (+4) oxidation state (Figs. 4a, b). The *in-situ/operando* XANES spectrum of SnO₂ exhibited a strong electrolyte-induced energy shift and fitting revealed a large fraction of metallic Sn. In contrast, the spectrum of FTO showed only a small energy shift at the reduction potential, indicating that the change in the oxidation state is extremely small. The linear combination fitting (LCF) results visually represent this trend more clearly (Fig. 4c, d).

The *in-situ/operando* Raman spectra, which show the chemical states of the surface, are shown in Fig. 4e, f. Carbon supports for the catalysts were not used for the *in-situ/operando* experiments to improve the peak intensity. The Raman peak at 630 cm⁻¹⁵³, which is associated with the symmetric stretching of Sn–O bonds (A_{1g} modes), was identical for SnO₂ and FTO, confirming the presence of oxide phase (Fig. 4a–d). This peak was observed for both SnO₂ and FTO at applied potentials above -0.8 V. However, for SnO₂, the Raman peak disappeared at a potential of -1 V, whereas for FTO, the Raman peak was still present at a potential of -1.2 V. These findings demonstrate that the surface of SnO₂ is converted to metallic Sn but the oxidized state of the FTO surface is maintained under high cathodic overpotentials, which is consistent with the *in-situ/operando* XANES results. Despite their similar radii, F ions have a higher electronegativity than O ions. This property would make F–Sn bonds stronger than O–Sn bonds, leading to enhanced stability of FTO. The behavior of SnO₂ and FTO catalysts for CO₂RR are summarized in Fig. 4e. SnO₂ catalysts exhibits good performance for formate production at low overpotential but are reduced to metallic Sn at high cathodic potentials, accelerating HER and lowering CO₂RR. On the other hand, FTO possess enhanced catalytic activity for CO₂ electro-reduction to formate by improving interaction with

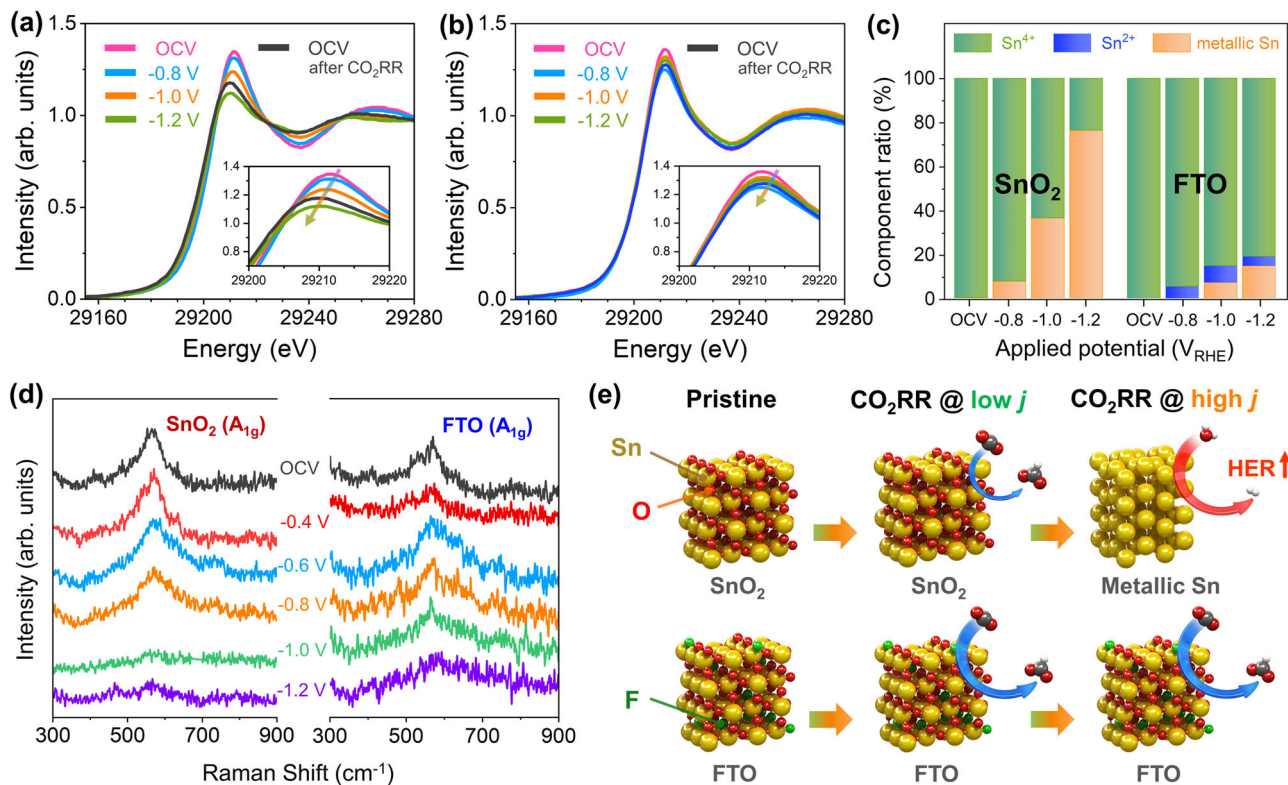


Fig. 4 *In-situ/operando* spectroscopy analyses for raveling origin of durability. **a, b** *In-situ/operando* Sn k-edge XANES spectra for **a** SnO₂/C and **b** FTO/C catalysts during CO₂RR in the flow-type electrolyzer and **c** its oxidation state distribution deconvoluted by linear combination fitting (orange: Sn, blue: Sn²⁺, and green: Sn⁴⁺). **d** *In-situ/operando* SER spectra obtained at constant potentials for SnO₂ and FTO catalysts without carbon supporter. Analyzed SER spectra present in the wavenumber region of 300–900 cm⁻¹. **e** Schematic illustration of reaction affinity for SnO₂ and FTO under low/high cathodic overpotential.

HCOO⁻. Furthermore, oxidation state of FTO stabilized by strong F–Sn bonds under high cathodic overpotentials contributes the enhanced current density and durability. Thus, we expect that the enhanced current density and durability of FTO could allow the development of economically feasible CO₂RR technology.

Discussion

In summary, we obtained insights into the performance of doped-SnO₂ catalysts for the CO₂RR to formate using a combination of flow-type single-cell experiments, *in-situ/operando* spectroscopy, and DFT calculations. Compared with traditional SnO₂ catalysts, the nanoparticles synthesized using TDA were much smaller because this surfactant prevents particle agglomeration during SnO₂ growth via micelle formation. The high dispersion of our SnO₂ catalysts allowed for a large number of oxide species to act as electrochemically active centers. The FTO/C catalyst exhibits higher performance than other doped catalysts, achieving partial current densities for formates of up to 330 mA cm⁻² and high faradaic efficiency (95% at 100 mA cm⁻²). Notably, using the FTO catalysts, we achieve superior formate selectivity (≈90%) over 7 days of operation at 100 mA cm⁻². Based on DFT calculation, fluorine doping not only enhance the interactions between HCOO⁻ and FTO surface but also alters electronic structure of CO₂ to facilitate electron transfer. Furthermore, *in-situ/operando* spectroscopy suggests that in FTO catalysts, oxidation state of Sn, which significantly affects the CO₂RR activity, did not change significantly under an applied potential. These findings suggest that fluorine dopant played an important role in increasing the selectivity for formate on the FTO catalyst by modulating electronic structure of Sn and enhancing the durability by preventing

reduction under reduction potentials. Our study provides insight for designing highly active and durable electrocatalysts for the electrochemical conversion of CO₂RR to formate.

Methods

Preparation of SnO₂ and doped-SnO₂ catalysts. To synthesize the SnO₂ and doped-SnO₂ catalysts, TDA (Sigma-Aldrich) was dissolved ultrasonically in a mixture of deionized water and ethanol. Then, SnCl₄ (Sigma-Aldrich) was added, and the mixture was stirred for 1 h. This suspension was ultrasonically blended with carbon black powder, and then ammonium hydroxide solution (NH₄OH, Sigma-Aldrich) was added dropwise, followed by stirring for 30 min. Subsequently, the suspension was refluxed at 80 °C for 72 h. The reaction mixture was cooled to room temperature, filtered, and washed several times with an ethanol solution. To remove excess TDA, the as-prepared SnO₂ catalyst was transferred to a glass-lined stainless-steel autoclave and hydrothermally treated at 120 °C for 24 h. A detailed description of the formation of the tin ethbutoxide intermediate in the ethanol solution and the formation of SnO₂ through the hydrolysis reaction is described in Supplementary Note 1. ATO, FTO, and ITO were synthesized using the same procedure, except that the composition of the metal precursor was varied by adding antimony acetate (C₆H₉O₆Sb, Sigma-Aldrich), ammonium fluoride (NH₄F, Sigma-Aldrich), and indium chloride (InCl₃, Sigma-Aldrich), respectively. Varying amounts of the dopant salts were added to 712 mg of SnCl₄ to synthesize the doped-SnO₂ sample. In ATO, 25.0 mg C₆H₉O₆Sb was used, in FTO, 19.48 g NH₄F, and in ITO, 109.6 g InCl₃. Antimony and indium were doped in the form of mixing Sb₂O₃ or In₂O₃ with SnO₂ during hydrolysis and condensation, respectively. On the other hand, fluorine was incorporated through oxygen substitution⁵⁴.

Preparation of SnO₂-based catalyst electrodes for the CO₂RR. A catalyst ink was prepared by ultrasonically mixing 5 wt% of ionomer solution (Dioxide, 15 wt% target of catalyst) and SnO₂-based catalyst powder (30 mg) with ethanol (2 mL). The SnO₂-based catalyst electrodes were fabricated by spraying the prepared catalyst ink onto a GDL (Sigracet 39 BB, SGL Carbon) at 70 °C. The electrode area was 2 cm² and the loading of SnO₂ was fixed at 0.5 mg cm⁻².

Preparation of Fe-Ni foam electrodes for the oxygen evolution reaction (OER) in alkaline. Fe-Ni foam electrodes for the OER were fabricated by a simple dip-

coating method. The Ni foam was washed with deionized water and dried under nitrogen. After dipping in a 0.125 M FeCl₃ solution, the Ni foam was removed and dried in a convection oven at 70 °C. The FeCl₃-coated Ni foam was then activated using a three-electrode system in 1 M KOH at a current density of 100 mA cm⁻² for 10 min. A graphite rod and Hg/HgO electrode were used as the counter and reference electrodes, respectively.

Preparation of IrO₂/Pt coated Ti-foam electrodes for the oxygen evolution reaction (OER in neutral). A catalyst ink was prepared by ultrasonically mixing 5 wt% of ionomer solution (Nafion, 10 wt% target of catalyst) and commercial iridium oxide catalyst powder (Alfa Aesar, 30 mg) with ethanol (2 mL). The electrodes were fabricated by spraying the prepared catalyst ink was onto a Pt coated Ti foam at 70 °C. The electrode area was 2 cm² and the loading of IrO₂ was fixed at 1 mg cm⁻². The reason of IrO₂ catalyst for OER in neutral electrolyte was described in Supplementary Note 2.

Electrochemical CO₂RR flow cell tests. A detailed schematic of the flow cell used for evaluating the electrochemical CO₂RR performance is shown in Supplementary Fig. 7. The fabricated SnO₂-based catalyst electrodes were used as the cathode. The active area of each electrode was 2 cm², and CO₂ as the reactant gas was fed into the serpentine flow field channel on the cathode side at a flow rate of 50 sccm. The electrolyte solution of 1 M KOH or 1 M KHCO₃ was supplied to both the anode and cathode sides using a pump. An AEM (Dioxide Materials, X37-50 Grade RT) was used to separate the anode and cathode flow channels. All electrochemical tests were conducted using a VSP potentiostat (BioLogic, VMP3B-10), which was suitable for measurements up to 10A. The reference electrode (Ag/AgCl, 3.5 M KCl) was inserted in the cathode flow line to measure and control the cathode potential.

The Faradaic efficiency of the catalyst was measured using GC and IC where points were taken at 18 min-intervals. The formate concentrations on the catholyte and anolyte were measured to calculate the total production of formate. The composition of the outlet gas was measured using gas chromatography (GC, Agilent 7890A). The inlet of the GC, fitted with a water trap to prevent water from entering the GC, was connected to the cathode outlet. Ultra-high-purity helium gas (99.9999%) was used as the carrier gas. A flame ionization detector and thermal conductivity detector were used to detect carbon-based gases (CO, CH₄, and C₂H₄) and hydrogen gas, respectively. A methanizer was used to enhance the detection of CO. The faradaic efficiency of each product was calculated using the following equation:

$$FE_{\text{product}}(\%) = \frac{i_{\text{product}}}{i_{\text{total}}} \times 100 = \frac{V_{\text{product}} \times Q \times \frac{2Fp}{RT}}{i_{\text{total}}} \times 100 \quad (3)$$

Where F is the Faraday constant (96485 C mol⁻¹), i is the flow rate of products, T is room temperature (298 K), and R is the ideal gas constant (8.314 J mol⁻¹ K⁻¹).

The total current was measured using a VSP potentiostat. The peaks in the GC chromatogram were used to determine the volumes of specific products, which allowed the partial current density of each product to be calculated. Ion chromatography (IC) coupled with inductively coupled plasma optical emission spectroscopy (Thermo Scientific, Dionex ICS-5000+ HPIC) was used to monitor formate, and FE_{formate} was calculated using the following equation:

$$FE_{\text{formate}}(\%) = \frac{i_{\text{formate}}}{i_{\text{total}}} \times 100 = \frac{C_{\text{formate}} \times N \times F}{i_{\text{total}}} \times 100 \quad (4)$$

where N is the number of electrons transferred and F is the Faraday constant. The peak in the IC chromatogram was used to determine the concentration of specific products.

Physical characterization. The microstructures of the synthesized catalysts were observed using HR-TEM (FEI Co, Titan 300 kV), and the elemental distribution in each catalyst was obtained using energy-dispersive X-ray spectrometry (FEI Co, Talos 200 kV). The nanoparticle size distributions were analyzed using ImageJ software, and the obtained profiles were fitted using a Gaussian function. Ten HR-TEM images were taken for each oxide sample, from which 300 particles were selected for particle size measurements. The surface chemistry of the catalysts was evaluated using X-ray photoelectron spectroscopy (Ulvac Co., PHI 5000 Versaprobe). Wide-angle XRD (Rigaku D-max/2500-PC, Cu-K α radiation) was used to investigate the crystal structure and identify the nature of the oxides. TGA (TA Instruments, Q600 SDT) of the catalysts was performed from room temperature to 800 °C at a rate of 10 °C min⁻¹. This analysis was performed in a N₂ atmosphere up to 500 °C, and O₂ gas was injected thereafter.

In-situ/operando X-ray absorption spectroscopy (XAS). The Sn k-edge hard-X-ray absorption spectroscopy (XAS) spectra of the synthesized catalysts were recorded at the 10C beamline of the Pohang Acceleration Laboratory (PAL). The setup for the *in-situ/operando* hard-XAS measurements with a homemade electrochemical single cell is shown in Supplementary Fig. 16. For *operando* XAS measurements, a 1-cm² hole was made in the anode and cathode bipolar plate and covered with Kapton film to allow passage of the X-rays. The operational conditions were the same as in the single-cell tests, and 1M KHCO₃ was used as the catholyte and anolyte. Before the XAS measurements, the electrode was stabilized

for 5 min at each potential. The hard-XAS analysis was carried out in the fluorescence collection mode using a Si (311) monochromator. The hard-XAS spectra were calibrated using Sn foil to ensure a zero shift in the edge energy. The XANES data were fitted using the Athena software (Demeter ver. 0.9.20). To maintain consistency in the analysis, the height of the arctangent function corresponding to the transition to the continuum level was set to one.

For the EXAFS analysis, Artemis (also implemented in Demeter ver. 0.9.20) software was utilized after the processing of data using the Athena software. The background signal was removed to extract the EXAFS signal for $R_{\text{bkg}} = 1.0\text{--}1.1 \text{ \AA}$. The EXAFS data were transformed using the Kaiser-Bessel function. The many-body reduction factor (S_0^2) for Sn was determined to be 0.86 from the EXAFS curve fit of the Sn foil. The statistical quality of the curve fit to the proposed models can be determined from the R-factor and χ^2 function available in the refinement.

In-situ/operando surface-enhanced Raman spectroscopy. The *in-situ/operando* surface-enhanced Raman spectroscopy (SERS) measurements for the gas-phase CO₂RR were performed using a homemade electrochemical three-electrode cell with a GDL, as shown in Supplementary Fig. 17. The excitation light source was a Nd:YAG laser (532 nm). A platinum wire was used as the counter electrode, Ag/AgCl (3.5 M KCl) was used as the reference electrode, and the catalyst-loaded GDL was used as the working electrode. For the CO₂RR, 100 sccm CO₂ was supplied to the catalyst-loaded GDL. The homemade electrochemical cell was filled to a thickness of 5 mm with 1 M KHCO₃ as the electrolyte. The electrochemical experiments were controlled using an IVIUM CompactStat.h potentiostat/galvanostat.

DFT calculations. DFT calculations were performed using the Quantum ESPRESSO package^{55,56}. Geometry optimization was performed using the Perdew-Burke-Ernzerhof functional⁵⁷ with the projector-augmented wave pseudopotentials^{58,59}. The Grimme's D3 (DFT-D3)⁶⁰ method was used to account for the van der Waals dispersion correction. A kinetic energy cutoff of 500 eV was used with a plane-wave basis set. Gaussian smearing was applied with a smearing width of 0.1 eV. The geometries were fully relaxed until the residual force on the atoms converged to 0.01 eV/Å. The SnO₂ (110) supercell was modeled using a unit cell of the tetragonal space group (mp-856) obtained from the Materials Project⁶¹. The four layers of the primitive unit cell that are cleaved to the (110) plane were expanded six times (2 × 3 × 4), yielding a supercell of 24 Sn and 48 O atoms with a lattice constant of 6.83 Å × 9.73 Å × 13.67 Å. To build the FTO (110) supercell, seven O atoms (~15%) were randomly replaced with F atoms. To simulate the SnO₂ and FTO crystal conditions under an applied potential of -1.0 V, the lattice constants of the SnO₂ and FTO (110) bulk were uniformly reduced by -1.37% and -0.33%, respectively (Supplementary Fig. 15 and Supplementary Table 1). The lattice constants of strained SnO₂ and FTO (110) bulk supercell were 6.74 Å × 9.60 Å × 13.48 Å and 6.81 Å × 9.70 Å × 13.62 Å, respectively. The Brillouin zone was sampled with a Monkhorst-Pack k-point mesh of (5 × 4 × 2) for bulk SnO₂ and FTO (110) supercells. To build the slab structure, a 20-Å vacuum gap was added along the c-axis of the stabilized supercells. The bottom two layers of the slab were fixed, while the top two layers were allowed to relax during geometry optimization. The Brillouin zone was sampled with a Monkhorst-Pack k-point mesh of (5 × 3 × 1) for SnO₂ and FTO (110) slab supercells.

The elementary steps of the electrochemical conversion reaction of CO₂ to HCOOH involving 2 electron pathway are described as follows:



where * represents the surface sites for molecule adsorption. The change in Gibbs free energy (ΔG) at 298 K and 1 atm was calculated through $\Delta G = \Delta E + \Delta ZPE - T\Delta S$, where ΔE is the total electronic energy obtained from the DFT optimization, ΔZPE is the change in the zero-point energies, T is the temperature, and ΔS is the change in entropy. The computational hydrogen electrode model⁶² was applied to calculate the chemical potential of proton/electron pairs, which is equal to the half of the chemical potential of H₂ gas under standard conditions and electrons with an applied bias of U ($-eU$). The pH contribution is considered by adding $k_B T \times \ln 10 \times \text{pH}$ to ΔG , where k_B is the Boltzmann constant. The ZPE and S of the molecules and adsorbates were determined from the calculated vibrational frequencies and NIST database^{63,64}, where all vibrations were treated in the harmonic oscillator approximation. The ZPE and S data are listed in Supplementary Tables 2 and 5, respectively.

Data availability

Source data are provided with this paper.

Received: 9 July 2021; Accepted: 8 March 2022;

Published online: 22 April 2022

References

- Mikkelsen, M., Jorgensen, M. & Krebs, F. C. The teraton challenge. A review of fixation and transformation of carbon dioxide. *Energy Environ. Sci.* **3**, 43–81 (2010).
- Nielsen, D. U., Hu, X. M., Daasbjerg, K. & Skrydstrup, T. Chemically and electrochemically catalysed conversion of CO₂ to CO with follow-up utilization to value-added chemicals (vol 1, pg 244, 2018). *Nat. Catal.* **2**, 95–95 (2019).
- Qiao, J. L., Liu, Y. Y., Hong, F. & Zhang, J. J. A review of catalysts for the electroreduction of carbon dioxide to produce low-carbon fuels. *Chem. Soc. Rev.* **43**, 631–675 (2014).
- Zhang, L., Zhao, Z. J. & Gong, J. L. Nanostructured materials for heterogeneous electrocatalytic CO₂ reduction and their related reaction mechanisms. *Angew. Chem. Int. Ed.* **56**, 11326–11353 (2017).
- Alvarez, A. et al. Challenges in the greener production of formates/formic acid, methanol, and DME by heterogeneously catalyzed CO₂ hydrogenation processes. *Chem. Rev.* **117**, 9804–9838 (2017).
- Verma, S., Kim, B., Jhong, H., Ma, S. C. & Kenis, P. J. A. A gross-margin model for defining techno-economic benchmarks in the electroreduction of CO₂. *Chemsuschem* **9**, 1972–1979 (2016).
- Li, Z. et al. Elucidation of the synergistic effect of dopants and vacancies on promoted selectivity for CO₂ electroreduction to formate. *Adv. Mater.* **33**, 2005113 (2021).
- Rabiee, H. et al. Tuning the product selectivity of the Cu hollow fiber gas diffusion electrode for efficient CO₂ reduction to formate by controlled surface Sn electrodeposition. *ACS Appl. Mater. Interfaces* **12**, 21670–21681 (2020).
- Lim, J., Kang, P. W., Jeon, S. S. & Lee, H. Electrochemically deposited Sn catalysts with dense tips on a gas diffusion electrode for electrochemical CO₂ reduction. *J. Mater. Chem. A* **8**, 9032–9038 (2020).
- Ye, K. et al. In situ reconstruction of a hierarchical Sn-Cu/SnO_x core/shell catalyst for high-performance CO₂ electroreduction. *Angew. Chem. Int. Ed.* **59**, 4814–4821 (2020).
- Tian, J. et al. Bi-Sn oxides for highly selective CO₂ electroreduction to formate in a wide potential window. *ChemSusChem* **14**, 2247–2254 (2021).
- Shen, S. et al. Stepped surface-rich copper fiber felt as an efficient electrocatalyst for the CO₂RR to formate. *J. Mater. Chem. A* **6**, 18960–18966 (2018).
- Jiang, B., Zhang, X.-G., Jiang, K., Wu, D.-Y. & Cai, W.-B. Boosting formate production in electrocatalytic CO₂ reduction over wide potential window on Pd surfaces. *J. Am. Chem. Soc.* **140**, 2880–2889 (2018).
- Han, N. et al. Ultrathin bismuth nanosheets from in situ topotactic transformation for selective electrocatalytic CO₂ reduction to formate. *Nat. Commun.* **9**, 1320 (2018).
- Tran-Phu, T. et al. Nanostructured β-Bi₂O₃ fractals on carbon fibers for highly selective CO₂ electroreduction to formate. *Adv. Funct. Mater.* **30**, 1906478 (2020).
- Fan, K. et al. Curved surface boosts electrochemical CO₂ reduction to formate via bismuth nanotubes in a wide potential window. *ACS Catal.* **10**, 358–364 (2019).
- Shi, Y. et al. Unveiling hydrocussite as an electrochemically stable active phase for efficient carbon dioxide electroreduction to formate. *Nat. Commun.* **11**, 1–10 (2020).
- Zhou, Y. et al. Mesoporous PdAg nanospheres for stable electrochemical CO₂ reduction to formate. *Adv. Mater.* **32**, 2000992 (2020).
- Han, N. et al. Alloyed palladium-silver nanowires enabling ultrastable carbon dioxide reduction to formate. *Adv. Mater.* **33**, 2005821 (2021).
- Wu, D., Huo, G., Chen, W., Fu, X.-Z. & Luo, J.-L. Boosting formate production at high current density from CO₂ electroreduction on defect-rich hierarchical mesoporous Bi/Bi₂O₃ junction nanosheets. *Appl. Catal. B Environ.* **271**, 118957 (2020).
- Grigioni, I. et al. CO₂ electroreduction to formate at a partial current density of 930 mA cm⁻² with InP colloidal quantum dot derived catalysts. *ACS Energy Lett.* **6**, 79–84 (2020).
- Trasatti, S. Work function, electronegativity, and electrochemical behavior of metals. 3 Electrolytic Hydrogen Evolution in Acid Solutions. *J. Electroanal. Chem.* **39**, 163–184 (1972).
- Zhu, Q. G. et al. Efficient Reduction of CO₂ into Formic Acid on a Lead or Tin Electrode using an Ionic Liquid Catholyte Mixture. *Angew. Chem. Int. Ed.* **55**, 9012–9016 (2016).
- Yang, Z. N., Oropeza, F. E. & Zhang, K. H. L. P-block metal-based (Sn, In, Bi, Pb) electrocatalysts for selective reduction of CO₂ to formate. *APL Mater* **8**, 060901 (2020).
- Xia, Z. et al. Highly selective electrochemical conversion of CO₂ to HCOOH on dendritic indium foams. *Chemelectrochem* **5**, 253–259 (2018).
- Haynes, W. M. *CRC Handbook of Chemistry and Physics, 97th Edition (CRC Handbook of Chemistry & Physics)* (CRC Press, 2016).
- Hou, X. et al. 3D core-shell porous-structured Cu@Sn hybrid electrodes with unprecedented selective CO₂-into-formate electroreduction achieving 100%. *J. Mater. Chem. A* **7**, 3197–3205 (2019).
- Zhang, Y., Zhang, X., Bond, A. M., & Zhang, J. Identification of a new substrate effect that enhances the electrocatalytic activity of dendritic tin in CO₂ reduction. *Phys. Chem. Chem. Phys.* **20**, 5936–5941 (2018).
- Kumar, B. et al. Reduced SnO₂ porous nanowires with a high density of grain boundaries as catalysts for efficient electrochemical CO₂-into-HCOOH conversion. *Angew. Chem. Int. Ed. Engl.* **56**, 3645–3649 (2017).
- Han, N. et al. Self-templated synthesis of hierarchical mesoporous SnO₂ nanosheets for selective CO₂ reduction. *J. Mater. Chem. A* **7**, 1267–1272 (2019).
- Zheng, X. et al. Sulfur-modulated tin sites enable highly selective electrochemical reduction of CO₂ to formate. *Joule* **1**, 794–805 (2017).
- Li, F. et al. Towards a better Sn: efficient electrocatalytic reduction of CO₂ to formate by Sn/SnS₂ derived from SnS₂ nanosheets. *Nano Energy* **31**, 270–277 (2017).
- Wen, G. et al. Orbital interactions in Bi-Sn bimetallic electrocatalysts for highly selective electrochemical CO₂ reduction toward formate production. *Adv. Energy Mater.* **8**, 1802427 (2018).
- Luc, W. et al. SO₂-induced selectivity change in CO₂ electroreduction. *J. Am. Chem. Soc.* **141**, 9902–9909 (2019).
- Liu, L.-X. et al. Tuning Sn₃O₄ for CO₂ reduction to formate with ultra-high current density. *Nano Energy* **77**, 105296 (2020).
- Sen, S., Brown, S. M., Leonard, M. & Brushett, F. R. Electroreduction of carbon dioxide to formate at high current densities using tin and tin oxide gas diffusion electrodes. *J. Appl. Electrochem.* **49**, 917–928 (2019).
- Qian, Y., Liu, Y., Tang, H. & Lin, B.-L. Highly efficient electroreduction of CO₂ to formate by nanorod@2D nanosheets SnO. *J. CO₂ Utilization* **42**, 101287 (2020).
- Chen, Y. et al. A robust, scalable platform for the electrochemical conversion of CO₂ to formate: identifying pathways to higher energy efficiencies. *ACS Energy Lett.* **5**, 1825–1833 (2020).
- Liang, C. et al. High efficiency electrochemical reduction of CO₂ beyond the two-electron transfer pathway on grain boundary rich ultra-small SnO₂ nanoparticles. *J. Mater. Chem. A* **6**, 10313–10319 (2018).
- Kopljär, D., Inan, A., Vindayer, P., Wagner, N. & Klemm, E. Electrochemical reduction of CO₂ to formate at high current density using gas diffusion electrodes. *J. Appl. Electrochem.* **44**, 1107–1116 (2014).
- Dutta, A. et al. Probing the chemical state of tin oxide NP catalysts during CO₂ electroreduction: a complementary operando approach. *Nano Energy* **53**, 828–840 (2018).
- Zhang, Y., Guo, S.-X., Zhang, X., Bond, A. M. & Zhang, J. Mechanistic understanding of the electrocatalytic CO₂ reduction reaction—New developments based on advanced instrumental techniques. *Nano Today* **31**, 100835 (2020).
- Baruch, M. F., Pander, J. E. III, White, J. L. & Bocarsly, A. B. Mechanistic insights into the reduction of CO₂ on tin electrodes using in situ ATR-IR spectroscopy. *ACS Catal.* **5**, 3148–3156 (2015).
- Díaz-Sainz, G. et al. Improving trade-offs in the figures of merit of gas-phase single-pass continuous CO₂ electrocatalytic reduction to formate. *Chem. Eng. J.* **405**, 126965 (2021).
- Vennekoetter, J.-B., Sengpiel, R. & Wessling, M. Beyond the catalyst: How electrode and reactor design determine the product spectrum during electrochemical CO₂ reduction. *Chem. Eng. J.* **364**, 89–101 (2019).
- Oh, H. S., Nong, H. N. & Strasser, P. Preparation of mesoporous Sb-, F-, and in-doped SnO₂ bulk powder with high surface area for use as catalyst supports in electrolytic cells. *Adv. Funct. Mater.* **25**, 1074–1081 (2015).
- Li, Y. F. et al. Realizing a SnO₂-based ultraviolet light-emitting diode via breaking the dipole-forbidden rule. *NPG Asia Mater* **4**, e30 (2012).
- Anaraki, E. H. Enhanced electron extraction using SnO₂ for high-efficiency planar-structure HC(NH₂)₂PbI₃-based perovskite solar cells. *Nat. Energy* **2**, 16177 (2017).
- Sun, S. H. et al. Raman scattering study of rutile SnO₂ nanobelts synthesized by thermal evaporation of Sn powders. *Chem. Phys. Lett.* **376**, 103–107 (2003).
- Xie, Q. X., Zhu, Y. T., Zhao, P., Zhang, Y. F. & Wu, S. H. One-pot hydrothermal fabrication and enhanced lithium storage capability of SnO₂ nanorods intertwined with carbon nanotubes and graphene nanosheets. *J. Mater. Sci.* **53**, 9206–9216 (2018).
- Wu, X. Y. et al. Ultrasmall SnO₂ nanocrystals with adjustable density embedded in N-doped hollow mesoporous carbon spheres as anode for Li+/Na+ batteries. *J. Mater. Sci.* **55**, 14464–14476 (2020).
- Burdyn, T. & Smith, W. A. CO₂ reduction on gas-diffusion electrodes and why catalytic performance must be assessed at commercially-relevant conditions. *Energy Environ. Sci.* **12**, 1442–1453 (2019).
- Aragon, F. H. et al. Evidences of the evolution from solid solution to surface segregation in Ni-doped SnO₂ nanoparticles using Raman spectroscopy. *J. Raman Spectrosc.* **42**, 1081–1086 (2011).
- Koo, B.-R., Oh, D.-H., Riu, D.-H. & Ahn, H.-J. Improvement of transparent conducting performance on oxygen-activated fluorine-doped tin oxide electrodes formed by horizontal ultrasonic spray pyrolysis deposition. *ACS Appl. Mater. Interfaces* **9**, 44584–44592 (2017).
- Giannozzi, P. et al. QUANTUM ESPRESSO: a modular and open-source software project for quantum simulations of materials. *J. Phys.-Condens. Matter* **21**, 395502 (2009).

56. Giannozzi, P. et al. Advanced capabilities for materials modelling with QUANTUM ESPRESSO. *J. Phys.-Condens. Matter* **29**, 465901 (2017).
57. Perdew, J. P., Burke, K. & Ernzerhof, M. Generalized gradient approximation made simple. *Phys. Rev. Lett.* **77**, 3865–3868 (1996).
58. Blochl, P. E. Projector augmented-wave method. *Phys. Rev. B* **50**, 17953–17979 (1994).
59. Dal Corso, A. Pseudopotentials periodic table: From H to Pu. *Comp. Mater. Sci.* **95**, 337–350 (2014).
60. Grimme, S., Antony, J., Ehrlich, S. & Krieg, H. A consistent and accurate ab initio parametrization of density functional dispersion correction (DFT-D) for the 94 elements H–Pu. *J. Chem. Phys.* **132**, 154104 (2010).
61. Jain, A. et al. Commentary: the materials project: a materials genome approach to accelerating materials innovation. *APL Mater.* **1**, 011002 (2013).
62. Peterson, A. A., Abild-Pedersen, F., Studt, F., Rossmeisl, J. & Norskov, J. K. How copper catalyzes the electroreduction of carbon dioxide into hydrocarbon fuels. *Energy Environ. Sci.* **3**, 1311–1315 (2010).
63. Bai, Y. H., Chen, B. W. J., Peng, G. W. & Mavrikakis, M. Density functional theory study of thermodynamic and kinetic isotope effects of H₂/D₂ dissociative adsorption on transition metals. *Catal. Sci. Technol.* **8**, 3321–3335 (2018).
64. NIST Computational Chemistry Comparison and Benchmark Database NIST Standard Reference Database Number 101 Release 21, August 2020, Editor: Russell D. Johnson III <http://cccbdb.nist.gov/> <https://doi.org/10.18434/T47C7Z>.

Acknowledgements

This work was supported by institutional program grants from the Korea Institute of Science and Technology and “Carbon to X Project” (Project No. 2020M3H7A1098229) through the National Research Foundation (NRF) funded by the Ministry of Science and ICT, Republic of Korea. This research was also supported by the National Research Council of Science & Technology (NST) grant by the Korean government (MSIT) (No. CAP21011-100), National Research Foundation of Korea (NRF) grant funded by the Korean government (MSIT) (NRF-2021R1A2C2093467), and National Supercomputing Center with supercomputing resources including technical support (KSC-2021-CRE-0284). We also acknowledge Advanced Analysis Center at KIST for the TEM and Raman measurements. We wish to thank 10C PAL beamline for measuring the hard X-ray absorption spectroscopy (XAS).

Author contributions

H.-S.O. and Y.-J.K. conceived the idea, designed the experiments, and supervised the work. D.K.L. designed/simulated the DFT calculations. J.-Y.K. synthesized the catalysts,

analyzed the data, and wrote the manuscript. W.H.L. conducted the electrochemical and in-situ experiments and wrote the manuscript. M.G.K. performed XANES analysis. J.P., Y.J., and B.K.M. contributed to the electrochemical analysis. T.-Y.S. and W.-S.L. contributed to the catalyst synthesis. All authors reviewed the manuscript and agreed with its content.

Competing interests

The authors declare no competing interests.

Additional information

Supplementary information The online version contains supplementary material available at <https://doi.org/10.1038/s41467-022-29783-7>.

Correspondence and requests for materials should be addressed to Young-Jin Ko, Dong Ki Lee or Hyung-Suk Oh.

Peer review information *Nature Communications* thanks the anonymous reviewers for their contribution to the peer review of this work. Peer reviewer reports are available.

Reprints and permission information is available at <http://www.nature.com/reprints>

Publisher's note Springer Nature remains neutral with regard to jurisdictional claims in published maps and institutional affiliations.



Open Access This article is licensed under a Creative Commons Attribution 4.0 International License, which permits use, sharing, adaptation, distribution and reproduction in any medium or format, as long as you give appropriate credit to the original author(s) and the source, provide a link to the Creative Commons license, and indicate if changes were made. The images or other third party material in this article are included in the article's Creative Commons license, unless indicated otherwise in a credit line to the material. If material is not included in the article's Creative Commons license and your intended use is not permitted by statutory regulation or exceeds the permitted use, you will need to obtain permission directly from the copyright holder. To view a copy of this license, visit <http://creativecommons.org/licenses/by/4.0/>.

© The Author(s) 2022